


Article

Changes in Precipitation Extremes over the Source Region of the Yellow River and Its Relationship with Teleconnection Patterns

Feifei Yuan ¹, Jiahong Liu ^{2,*}, Ronny Berndtsson ³, Zhenchun Hao ¹, Qing Cao ¹, Huimin Wang ¹, Yiheng Du ³ and Dong An ³

¹ State Key Laboratory of Hydrology-Water Resources and Hydraulic Engineering, Hohai University, Nanjing 210098, China; ffei.yuan@gmail.com (F.Y.); hzchun@hhu.edu.cn (Z.H.); qingcaohhu@163.com (Q.C.); hmwang@hhu.edu.cn (H.W.)

² State Key Laboratory of Simulation and Regulation of Water Cycle in River Basin, China Institute of Water Resources and Hydropower Research, Beijing 100038, China

³ Department of Water Resources Engineering, Lund University, 22100 Lund, Sweden; ronny.berndtsson@tvrl.lth.se (R.B.); yiheng.du@tvrl.lth.se (Y.D.); dong.an@tvrl.lth.se (D.A.)

* Correspondence: liujh@iwhr.com; Tel.: +86-10-6878-1936

Received: 3 February 2020; Accepted: 26 March 2020; Published: 30 March 2020



Abstract: Precipitation extremes and their underlying causes are important processes to understand to plan appropriate adaptation measures. This paper presents an analysis of the spatiotemporal variability and trend of precipitation extremes in the important source region of the Yellow River and explores the connection to global teleconnection patterns and the 850-mb vector wind. Six indices for precipitation extremes were computed and analyzed for assessment of a changing regional climate. Results showed that these indices have a strong gradient from the northwest to the southeast part for the period 1961–2015, due to the great influence from the south-easterly summer monsoon flow. However, no statistically significant trends were found for the defined indices at the majority of stations, and their spatial distribution are noticed by irregularly mixed positive and negative changes except for the maximum number of consecutive wet days (CWD). Singular value decomposition analysis revealed that the precipitation extreme indices—including annual total precipitation when daily precipitation >95th percentile (R95p), annual count of days with daily precipitation ≥ 10 mm (R10mm), annual maximum consecutive 5-day precipitation (R5d), total precipitation divided by the number of wet days (SDII), and CWD—are negatively related to the El Nino-Southern Oscillation (NINO 3.4) in the first mode, and the maximum number of consecutive dry days (CDD) is positively related to the Scandinavian pattern in the second mode at 0.05 significance level. The 850-mb vector wind analysis showed that the southwestern monsoon originating from the Indian Ocean brings sufficient moisture to this region. Furthermore, the anti-cyclone in the western part of the North Pacific plays a significant role in the transport of moisture to the source region of the Yellow River. The links between precipitation extremes and teleconnection patterns explored in this study are important for better prediction and preparedness of climatic extremes.

Keywords: precipitation extremes; teleconnection patterns; wind vector; the source region of the Yellow River

1. Introduction

The Yellow River Basin has experienced major floods and droughts that have caused devastating damages in recent years. This region is more fragile and vulnerable to climate extremes due to population growth, aging infrastructure and urbanization development [1–3]. The source region of

the Yellow River (SRYR) produced one third of the whole basin's streamflow, and climate change and climate variability are expected to largely influence the precipitation in this region, and impose stress on the water resources [4]. Precipitation extremes have increased in intensity and frequency under global warming [5–7], and this change has significant impact on the natural habitats of human communities in terms of property damage, loss of life and endangered species. It has been a fundamental issue for the government, the public and the research community due to the disastrous consequences [8–12]. Hence, understanding extreme climatic events is an important goal for water managers and policy makers in order to identify and mitigate the risks and the resulting hydrologic responses.

Teleconnection patterns are recurring, persistent and large-scale oscillating circulation systems in the atmosphere, which are identified as modes of low-frequency pressure variability. They are strongly linked to the local and regional extreme hydro-climatic events at different places in the world [13,14]. Teleconnections can be defined as the statistical relationships for climate variables at different locations, and the spatiotemporal aspects of teleconnections can be explained by the dynamical structure of the atmosphere [15]. Researches have shown that teleconnection patterns have strong influence on the hydro-climatic variabilities at different spatiotemporal scales [8,16]. The relationship between the wind vector and precipitation has often been analyzed to explore possible mechanisms of precipitation variability [17,18]. Studies have demonstrated that the composite distribution of atmospheric circulation and monsoon variability, as affected by wind anomalies at the 850-mb, can explain precipitation anomalies in China [19,20].

Some research has contributed to long-term precipitation change using observational data in the SRYR with a focus on changes in mean values [21–24]. Research recently has tried to establish the links between global atmospheric circulation and local hydrological events [25–29]. Krichak, et al. [30] explored teleconnection relationships with precipitation extremes in the Mediterranean region. They found that the interannual variability of the frequency of days with heavy precipitation was affected by the teleconnections influence on the spatial patterns in the regions with enhanced potential vorticity of air moisture. Casanueva et al. [8] displayed significant relationships between the Atlantic Multidecadal Oscillation and R95p. Hatzaki et al. [14] examined the influence of Eastern Mediterranean pattern on the duration, frequency, and intensity of precipitation extremes. Wang et al. [31] presented the observational evidence to show that ENSO has a strong influence on China's climate. Zhang et al. [32] examined the wind anomaly at 850-mb to identify large-scale atmospheric circulation patterns for annual and seasonal precipitation changes in the Yangtze River basin. Hellstrom [33] identified the 850-mb wind for precipitation extremes in Sweden. Yang et al. [34] established the possible links between precipitation extremes and climate patterns in the Pearl River Basin.

In view of the above, the investigations of precipitation extremes changes are quite limited in the SRYR. The precipitation extremes in the SRYR can be possibly explained by examining its connections with teleconnection patterns and analyzing the 850-mb wind vector. To the authors' knowledge, this has not been investigated and analyzed in detail in relation to results from previous studies. Hence, this research comprehensively examines the spatial and temporal features of precipitation extremes considering precipitation percentile, intensity and persistence by trend analysis methods. Most importantly, this work improves the knowledge by exploring the physical mechanisms of change in precipitation extremes in the SRYR through its linkage to global teleconnection patterns. Furthermore, the association between the 850-mb wind vector and precipitation extremes in the SRYR was examined to improve our physical understanding of hydrological processes in this region. It is significant to identify the above relationships for the SRYR as they have major implications on ecological sustainability, disaster control and integrated water resources planning and implementation. It could also be helpful for projecting the frequency and severity of precipitation extremes in the SRYR.

2. Study Area and Methods

2.1. Study Area and Data

The SRYR ($32^{\circ}12'–35^{\circ}48' N$ and $95^{\circ}50'–103^{\circ}28' E$) is located on the northeast Qinghai-Tibet Plateau with an area of $12.2 \times 10^4 \text{ km}^2$ covering 16% of the whole river basin. It is characterized by the significant altitude variation from 2670 m to 6253 m (Figure 1), which contributes significantly to the spatiotemporal hydro-climatic variability. Climatologically, the SRYR is recognized as a semi-humid region. In the cold season, the dominant climate is governed by the arid north-western environment and cold moist air [35]. In the warm season, the southwest monsoon from the Indian Ocean brings abundant warm vapor to the SRYR, forming the Plateau's humid monsoon climate [36]. Average annual precipitation decreases from the southeast to the northwest ranging from 300 to 750 mm. About 75% of the annual precipitation falls between June and September. The characteristics of precipitation in the SRYR are long duration, low intensity and large area coverage [36].

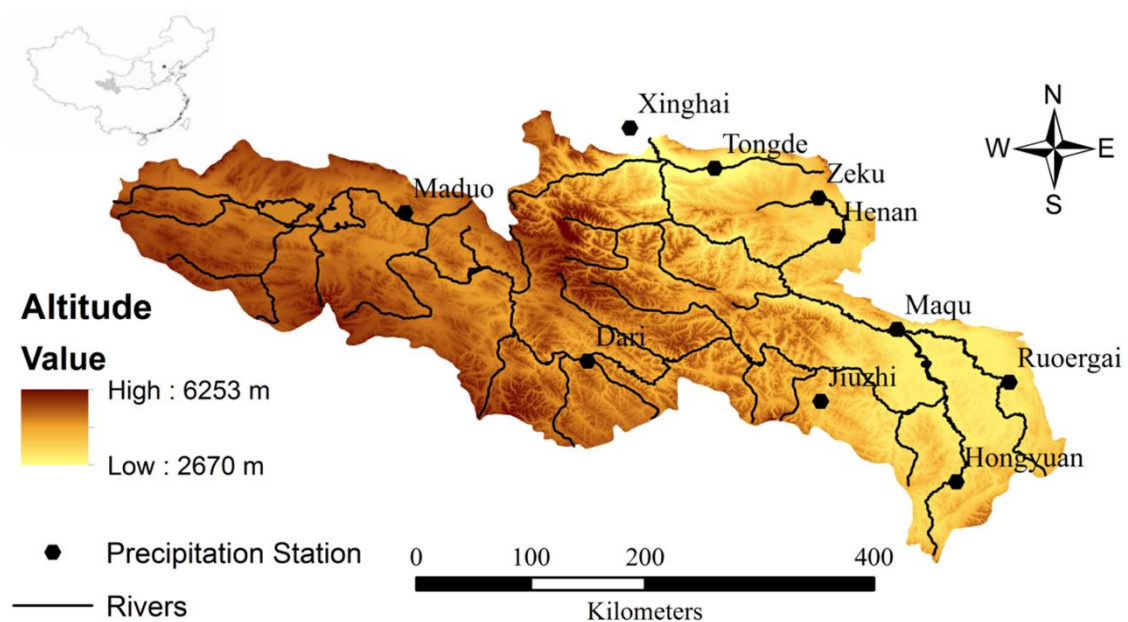


Figure 1. Precipitation stations, river network and topography in the SRYR.

Daily precipitation at ten meteorological stations in this region were acquired from the China Meteorological Administration (Figure 1). The data period is from 1961 to 2015, except for the Tongde and Zeku stations where the data period is from 1961 to 2010. The data continuity and quality have been verified by the above administration. Based on the impact of possible related teleconnection patterns on the precipitation in China and data availability, ten monthly climate indices data for different teleconnection patterns, including El Nino-Southern Oscillation (NINO 3.4), North Atlantic Oscillation (NAO), Polar/Eurasia Pattern (POL), East Atlantic Pattern (EA), West Pacific Pattern (WP), East Atlantic/West Russian Pattern (EA/WR), Pacific/North American Pattern (PNA), Scandinavian Pattern (SCA), India Ocean Dipole (IOD), and Pacific Decadal Oscillation (PDO), were accessed from the Climate Prediction Centre (NOAA). Detailed description of the above teleconnection patterns could be checked in the research by Washington et al. [37] and Barnston and Livezey [38]. The 850-mb vector wind reanalysis data for the period of 1961–2015 from the National Center for Environmental Prediction (NCEP)/the National Center for Atmospheric Research (NCAR) were used to explore the possible underlying reasoning of the spatiotemporal features of precipitation extremes (<https://www.esrl.noaa.gov/psd/data/gridded/data.ncep.reanalysis.html>).

2.2. Methods

2.2.1. Precipitation Extreme Indices

To be able to evaluate the frequency and intensity of extreme weather, a set of extreme climate indices are formulated and coordinated by ETCCDI (<http://etccdi.pacificclimate.org/indices.shtml>). Consequently, the above extreme indices were developed so that researchers worldwide can calculate the indices in exactly the same way, such that their analyses will fit seamlessly into the global climate change picture [39]. It should also be noted that one of major problems for extremes is that they are particularly sensitive to “scaling issues” in which there is a fundamental mismatch between the spatial representativeness of point-based and gridded values [40]. Numerous researches have used these defined indices for extreme climate research [6,8,41]. Table 1 shows the precipitation extreme indices used here. Six precipitation extreme indices based on the daily precipitation data were computed and examined. The selected indices were used for assessing an extreme climate considering the precipitation robust statistical properties, including percentile, intensity and persistence. The upper fifth percentile (R95p) indicates the total precipitation of very wet days. Extreme events exceeding precipitation absolute thresholds are defined by the count of days with heavy precipitation larger than 10 mm (R10mm). Cumulates for consecutive days are assessed by annual maximum 5-day precipitation total (R5d). Precipitation characteristics of daily intensity is represented by SDII. CDD and CWD are computed annually and they are for exploring durational aspects of extreme climate.

Table 1. Six precipitation extreme indices selected in this research. RR means daily precipitation. A wet day is defined as $RR \geq 1$ mm, and a dry day is defined as $RR < 1$ mm.

Category	Index	Description	Unit
Precipitation percentile	R95p	Annual total precipitation when $RR > 95$ th percentile	mm
	R10mm	Annual number of days with $RR \geq 10$ mm	days
Precipitation intensity	R5d	Annual maximum consecutive 5-day precipitation	mm
	SDII	Total precipitation divided by the number of wet days	mm/day
Precipitation persistence	CDD	Maximum number of consecutive dry days	days
	CWD	Maximum number of consecutive wet days	days

2.2.2. Trend Analysis

The characteristics of trend and variability in precipitation extreme indices for the period of 1961–2015 in the SRYR were investigated through linear regression and the Mann-Kendall test. Due to the limited and unevenly distributed stations in the SRYR, Thiessen polygon method was used to assess the regional trend in order to obtain a general picture of precipitation extreme changes in this region. The Mann-Kendall test is non-parametric, and it is a function of the ranks of the data series, indicating that it is not influenced by the data distribution and is insensitive to the outliers. The Mann-Kendall test could examine the trend of the data series, however, the magnitude of trends were also determined using Theil–Sen approach in some research [42]. Statistical level of significance was examined at the 0.05 for the trend test.

2.2.3. Analysis on the Teleconnections

Singular value decomposition (SVD) as the multivariate data analysis method is widely used to reveal the relationship between two different datasets in hydrological and meteorological studies [28,43,44]. The method can extract the dominant modes from the two analyzed datasets that are allowed to be regular or irregular. This is of great importance since the dominant modes of covariance are often associated with the physical interpretation. SVD is the diagonalization of the cross-covariance matrix between two datasets and reveals corresponding spatial distributions with a

few pairs of eigenvectors explaining the most variance [28,45]. In this study, SVD was conducted on the cross-covariance matrix of six precipitation extreme indices and ten climatic indices using annual data series for the same period. The annual climate indices were calculated by the sum of the monthly data, and both matrices are composed of the column vectors of the two different indices. The means of the variables were removed, and then the data matrix was standardized. The conduction of SVD produced two matrices of singular vectors and one set of singular values. A singular vector pair describes spatial patterns for each field that has overall covariance given by the corresponding singular value [46]. Each mode of the optimally related patterns was characterized by the normalized squared covariance, which ranged from 0, where the two fields are not related, to 1, when the variations are perfectly correlated [46]. The mode included a pair of two optimally related time series, one for the precipitation extremes and the other for climate indices. The modes with most normalized squared covariance in this research were visually presented to compare the relationship between variations in climate indices and precipitation extreme indices variability.

From the singular vector pairs of the cross-covariance matrix, the temporal expansion series of each field was acquired through projecting the data onto the appropriate singular vector. The so-called heterogeneous correlation maps from the above represent the correlation coefficients between the variables of one field (precipitation extreme indices) and the singular vector of the other field (climate indices) [46]. In our case, the heterogeneous correlation indicates how well the pattern of the precipitation extremes relate to the corresponding singular vector of climate indices. The different heterogeneous patterns are mutually orthogonal in the space domain [46]. The correlation coefficients were also shown to indicate the strength of the relationship between the two fields. This can be used to compare the relative importance of a particular mode in the expansion. A detailed statistical description can be seen in Wallace et al. [45] and Bretherton et al. [47].

3. Results and Discussion

Figure 2 presents the spatiotemporal pattern of precipitation extreme indices in the SRYR for the period 1961–2015. An increasing gradient from the northwest to the southeast part in the SRYR can be clearly seen for the R95p, R10mm, R5d, SDII, and CWD. Compared to the above five indices, the CDD has an opposite trend. This is due to the topographical gradient of precipitation and the annual precipitation distribution being largely affected by the south-easterly summer monsoon [21]. Hu et al. [36] reported that the precipitation intensity indices are in general related to the heavy rainfall events in the SRYR. R95p increases from the northwest to the southeast ranging from 59.2 mm to 142.3 mm. R5d shows an increasing trend from 39.9 mm in the northwest to 72.5 mm in the southeast, which agrees with the spatial feature of R10mm with 6–23 days. SDII has a relatively even distribution and the majority of stations have a value from 5.2 to 6.5 mm. The CWD is, at most stations, less than 8 days. CDD decreases from 105 days in the northwest to 42 days in the southeast. It is clear that the above indices change with regard to the precipitation amount, while intensity and duration have been spatially coherent over the SRYR due to the monsoon effect.

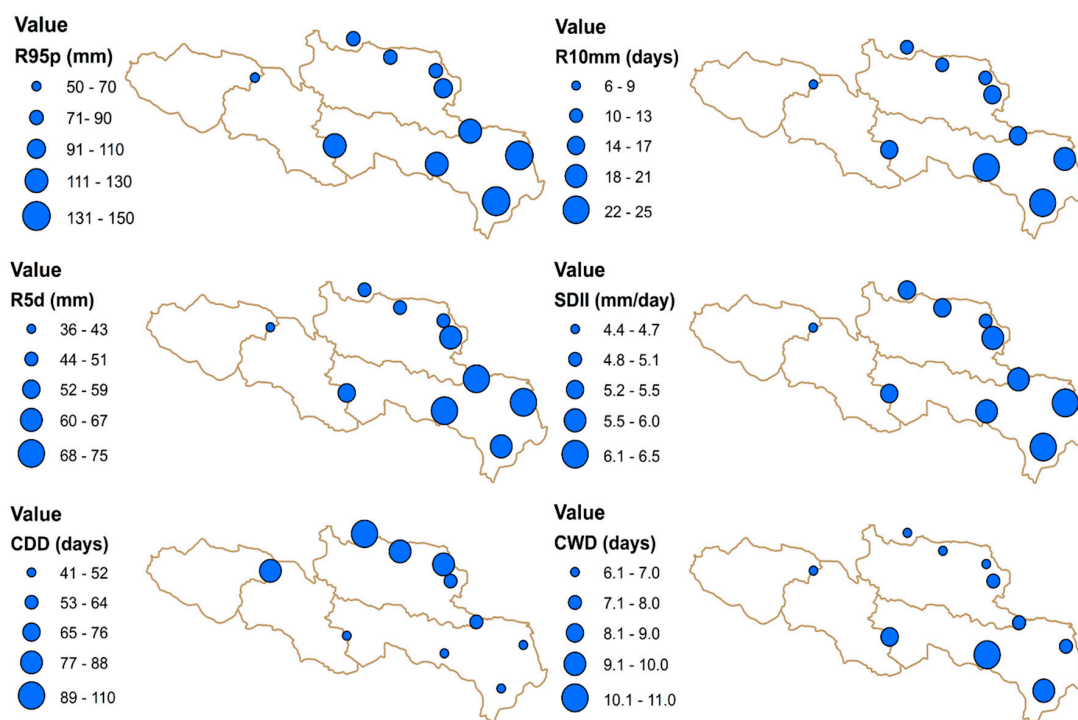


Figure 2. Spatiotemporal variability of precipitation extreme indices in SRYR during 1961–2015.

Figure 3 shows the precipitation extreme indices trend for the period of 1961–2015 in SRYR. Although most stations do not exhibit statistically significant trends for the six precipitation extreme indices, some spatial variations are detected. However, Fu et al. [48] found that the whole Yellow River Basin had experienced a decreasing trend of extreme precipitation events during the period 1961–2009. Dong et al. [49] revealed that extreme precipitation showed a significant negative trend in the mid-to-lower reaches of the Yellow River. No statistically significant trend is seen for R95p and CDD at all stations. Few stations show statistically significant decreasing trend for R10mm, R5d, and CWD. SDII has a mixed pattern of statistically significant trends. In general, the trends of the indices show a mix of upward and downward features except for the CWD. R95p, R10mm, R5d, and SDII display a mixed and irregular upward and downward trend, and the number of stations in both positive trend and negative trend is similar. This agrees with the previous research by Wang et al. [50] on changes in precipitation extremes in the Yellow River Basin for the period 1959–2008. Seasonal analysis by Hu et al. [36] indicated an increasing trend in the R5d index in winter. Li et al. [51] examined that precipitation-based indicators showed more mixed patterns of change and few stations had significant trends on the Loess Plateau of China. CDD shows a generally decreasing trend except for one station. All stations for CWD display a decreasing trend.

Table 2 presents the regional and stationary linear trends quantitatively. The data series of annual regional precipitation extreme indices, with statistically significant level at 0.05, are shown in Figure 4. Statistical level of significance was examined at 0.05 for the trend test. Both the precipitation percentile (R95p) and precipitation intensity (R10mm, R5d, and SDII) had slightly increasing trends. Wang et al. [50] showed that the regional average series of R95p, R10mm, and R5d had consistent negative trends across the Yellow River Basin. However, our analysis on the SRYR reveals an opposite trend. Both CDD and CWD indicate precipitation persistence with decreasing trends of -2.3 and -0.2 days/decade, respectively.

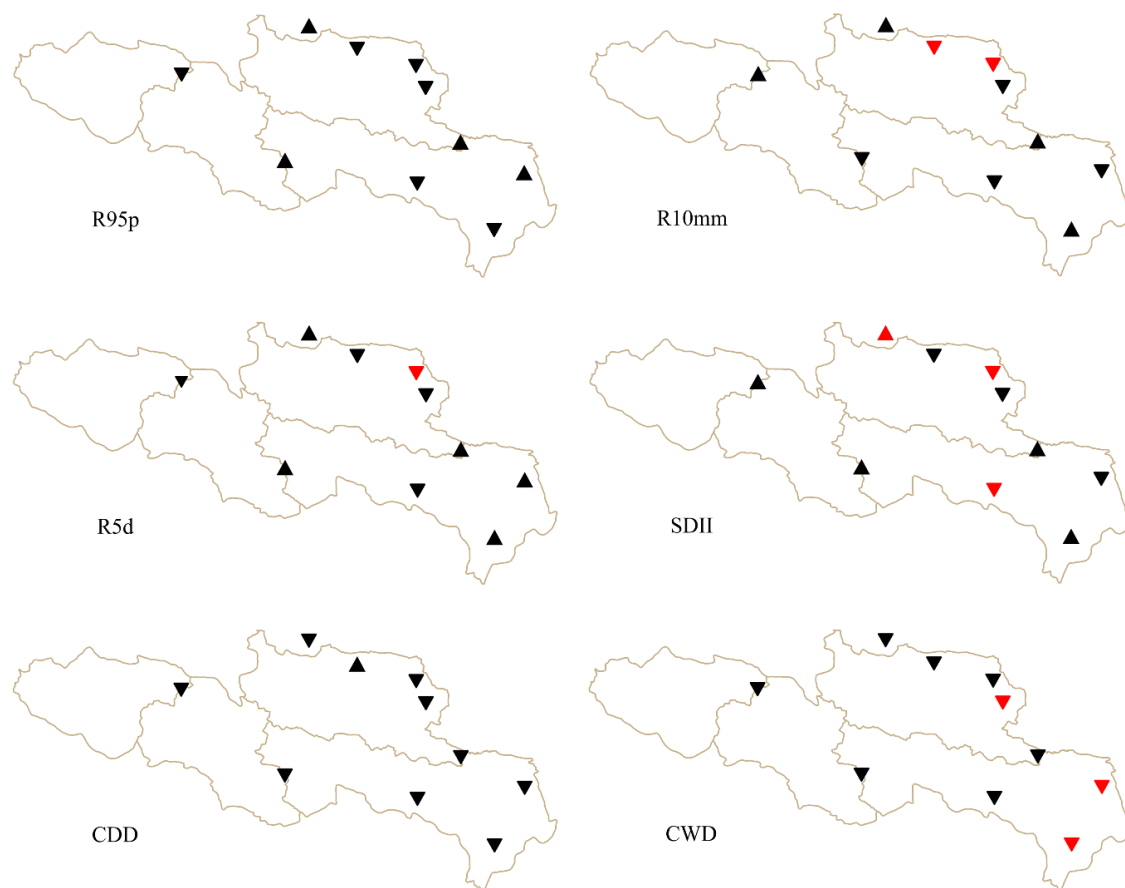


Figure 3. Precipitation extremes trends for the period 1961–2015 in the SRYR. The increasing (decreasing) trends are marked by upward (downward) triangles. Statistically significant trends are marked by red triangles.

Table 2. Regional and stationary linear trend of precipitation extremes indices.

Station/Indices	R95p (mm/decade)	R10mm (days/decade)	R5d (mm/decade)	SDII (mm/decade)	CDD (days/decade)	CWD (days/decade)
Hongyuan	−2.33	0.38	0.49	0.08	−1.16	−0.54
Ruoergai	1.44	−0.35	1.21	−0.01	−0.92	−0.40
Maqu	4.65	0.33	1.39	0.03	−2.50	−0.12
Jiuzhi	−7.34	−0.53	−3.36	−0.15	−2.92	−0.09
Henan	−3.48	−0.33	−1.98	−0.05	−2.41	−0.37
Dari	3.60	−0.02	0.88	0.03	−1.20	−0.07
Maduo	−0.09	0.12	−0.25	0.02	−5.64	−0.25
Xinghai	2.88	0.29	0.12	0.12	−2.48	−0.23
Zeku	−6.58	−1.80	−6.25	−0.21	−8.02	−0.25
Tongde	−5.65	−0.64	−2.29	−0.10	5.50	−0.20
Whole Region	0.85	0.09	0.15	0.02	−2.31	−0.20

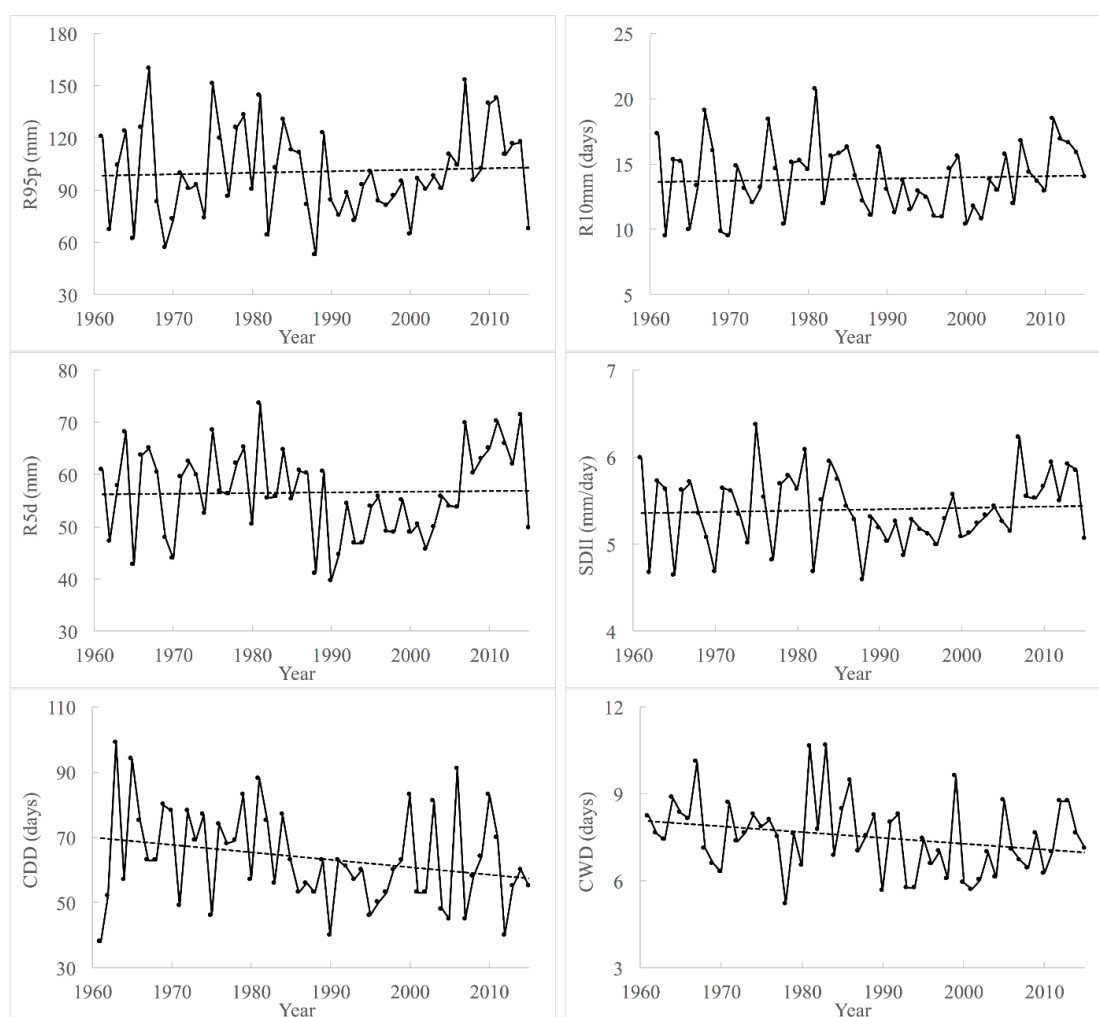


Figure 4. Time series for annual regional precipitation extreme indices. The dashed lines show the linear trend.

To identify the influence of global large-scale circulation on extreme precipitation in the SYRY, the cross-variance matrix of six annual regional precipitation extremes and ten climate indices from 1961 to 2015 were considered for the SVD calculation. Figure 5 shows the data series of different indices in the first two modes from the SVD output. It is noticed that only the first two modes are statistically significant, and they have the most explained variance with 62 and 37%, respectively. Hence, the first two modes accounting for 99% of explained variability can most easily be associated to physical phenomena and further clarify the spatiotemporal difference of precipitation extremes. The similar trend and variability in time series shows that precipitation extremes can be physically interpreted from the teleconnection patterns. The teleconnection influence for precipitation extremes in the SYRY can be attributed to two main factors: The geographic location and the difference in precipitation extremes variability. Since the two modes are orthogonal, meaning that the precipitation extremes variability in this region are diverse and should be analyzed separately. To be able to quantitatively examine the relationship between precipitation extreme indices and climate indices, Table 3 presents the corresponding heterogeneous correlation of different indices for the first two modes. It is noteworthy that the precipitation extreme indices including R95p, R10mm, R5d, SDII, and CWD are negatively related to NINO 3.4 in the first mode, and the CDD is positively related to the SCA in the second mode at 0.05 significance level. Hence, the first mode is dominated by the covariability between the above five precipitation extremes and NINO 3.4, and the second mode highlights the covariability between

the CDD and the SCA. Overall, the interannual variability of precipitation extremes in the SRYR can be explained by the ENSO and SCA events.

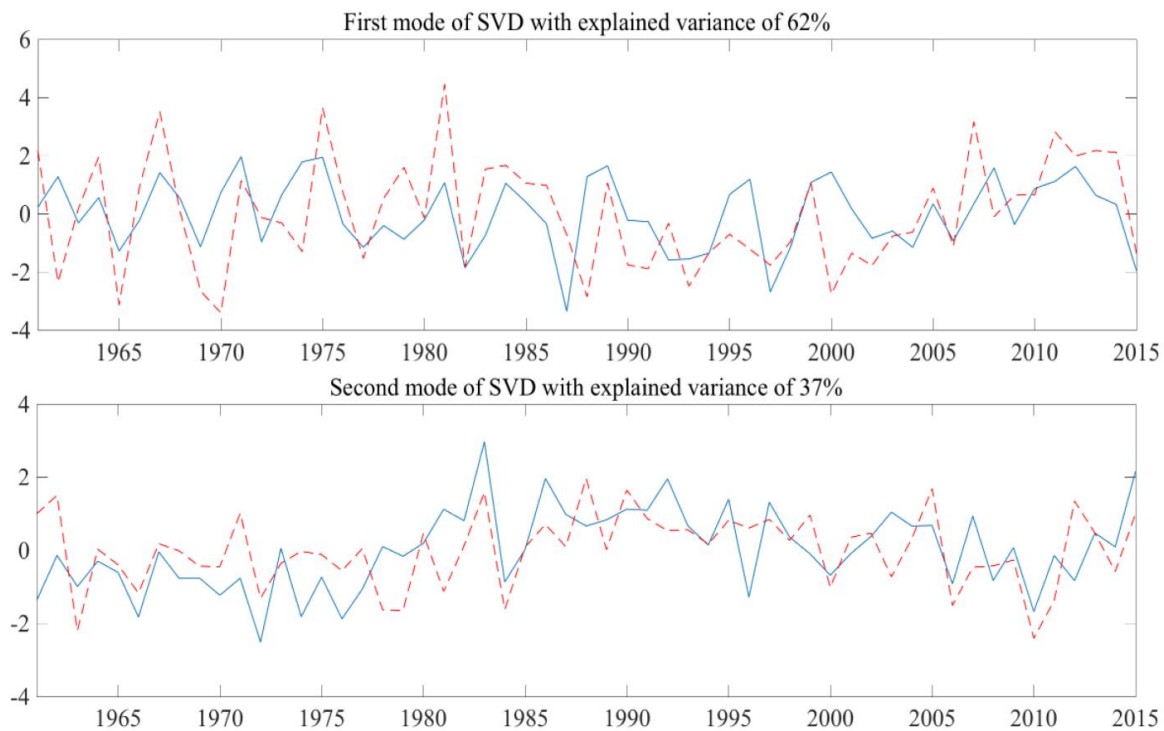


Figure 5. Time series of precipitation extreme indices (blue line) and climate indices (dashed red line) for the first and second modes of SVD.

Table 3. Heterogeneous correlation between precipitation extreme indices and climate indices (statistically significant values at the 0.05 level are in bold).

Mode	R95p	R10mm	R5d	SDII	CDD	CWD	NAO	EA	WP	PNA	EA/WR	SCA	POL	PDO	NINO 3.4	IOD
Mode 1	0.36	0.37	0.31	0.32	-0.11	0.26	0.04	-0.03	-0.20	-0.04	-0.15	-0.06	0.04	-0.16	-0.36	-0.09
Mode 2	-0.09	0.10	-0.18	-0.11	-0.36	0.19	0.21	0.03	-0.13	0.12	0.09	-0.41	0.04	0.13	0.08	-0.09

Numerous studies have worked on the influence of teleconnections on precipitation in the Yellow River. To illustrate the effects of ENSO and SCA influence on precipitation extremes in the SRYR, Figure 6 presents the spatial correlation between precipitation extreme indices and significantly correlated climate indices from the SVD results. The Pearson correlation coefficients between R95p, R10mm, R5d, SDII, and CWD and NINO 3.4 were calculated. The Pearson correlation coefficients between CDD and SCA were calculated. Positive correlations were detected for CDD, and dominant negative values were found for the other five indices. This is in accordance with the SVD results. No spatially coherent changes were found in general. However, high correlation can be seen in the north part of SRYR for CDD. The correlation coefficients have a decreasing trend for SDII from the northwest to southeast.

It is well known that ENSO has a significant impact on the East Asian monsoon, and hence further influence the precipitation in China. The spatial and temporal variability of extreme precipitation over China was highly affected by ENSO, the intensity of East Asian Monsoon and wind circulations in the region. The summer rainfall from June to September in the SRYR has strong links with global sea surface temperature, and higher sea surface temperature in equatorial Pacific Ocean during the El Nino phase is in correspondence with less summer rainfall [26]. This explains the negative association between the several investigated precipitation indices and NINO 3.4. Bueh and Nakamura [52] investigated the physical characteristics of the SCA and its influence on the Eurasian hydroclimate.

Zhang [53] pointed out that the accumulated cold air that spilled out south-eastwards, caused a severe cold wave in north China and Mongolia, and a record-breaking snowstorm when the SCA pattern weakened temporarily during the winter time. Liu et al. [54] showed that precipitation in central Asia has about 10% less than the average during the positive phase of the SCA. Our results suggest that SCA has a positive linkage with the consecutive drought in the second mode. The findings from this work verify the linkages between precipitation extremes and large-scale atmospheric circulation and also make contribution to the spatial distribution of associations over the SRYR.

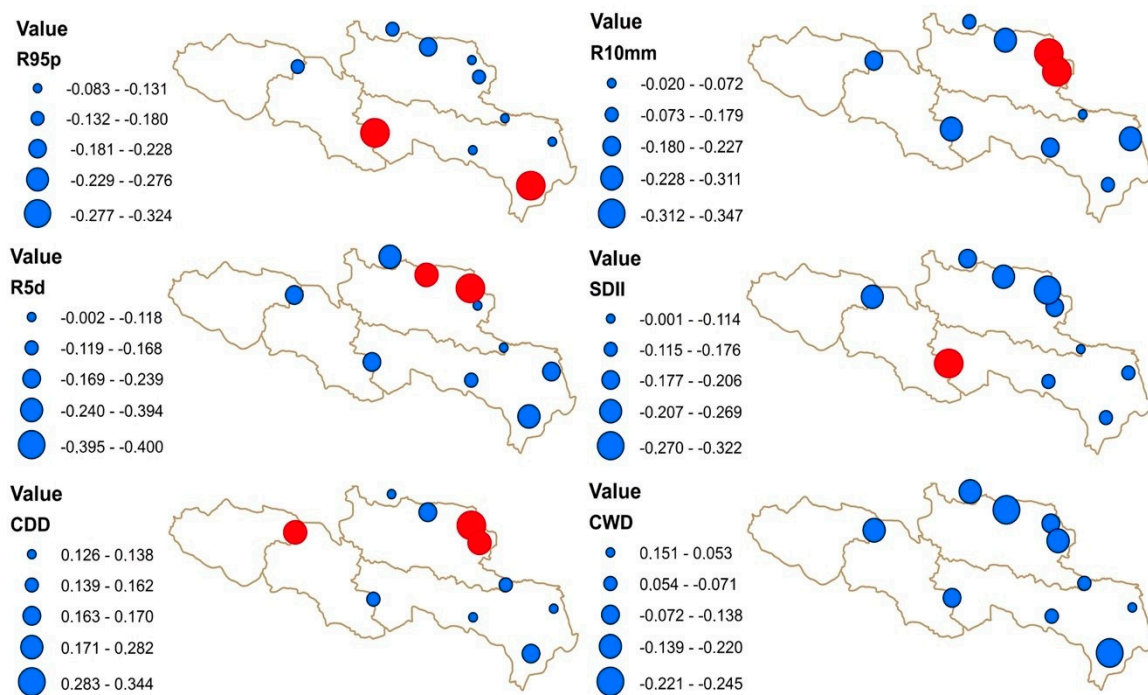


Figure 6. The spatial Pearson correlation between precipitation extreme indices and significantly related climate indices from the SVD results for the period between 1961–2015. Statistically significant trends are marked by red circles.

Figure 7 shows the 850-mb vector wind from June to September for the period of 1961–2015 to investigate possible underlying reasoning of variability for precipitation extremes in the SRYR. The 850-mb wind variability is associated with water vapor movement from the west part of the tropical Pacific to China, and it is a significant indicator for the precipitation intensity [55–57]. It can be pointed out that the southwestern monsoon from the Indian Ocean brings plentiful moisture to this region. Furthermore, the anti-cyclone in the western part of the North Pacific (WNP) also has a crucial impact in the transport of moisture to SRYR. The precipitation variability in the SRYR is dominated by the monsoon from the Indian Ocean and anti-cyclone in the WNP region, which coincides with the results from Huang et al. [58] and Liu et al. [59].

The large-scale atmospheric circulation and the Asian monsoon are related to ENSO intensity and variability, which have a large impact on precipitation patterns in China [60–65]. The physical reasoning for the relationship between precipitation and ENSO regimes can be explained through characteristics of circulation and monsoon [66]. Feng et al. [57] found that precipitation variability in China was mainly caused by anti-cyclonic flow in the WNP, connected with ENSO and ENSO Modoki events. Wang et al. [67] reasoned in a similar manner, that ENSO activities highly affect the local precipitation variability in the Yellow River Basin. Achuthavarier et al. [68] examined the role of the Indian Ocean in the ENSO-Indian summer monsoon teleconnection, and found out that ENSO-induced sea surface temperature forms a strong dipole pattern oriented along the zonal direction in the Indian Ocean, preventing the ENSO signals from reaching the Indian monsoon region. Ashok et al. [69]

examined that the Indian Ocean Dipole plays an important role in the correlation between the ENSO and Indian Ocean Monsoon. Feng and Hu [70] investigated that the monsoon from the Indian Ocean connects and regulates the ENSO effect on summer rainfall in northern China. It can be pointed out that the effect of atmospheric circulation and monsoon on precipitation extremes in the SRYR is related to ENSO variability, considering the high correlation between NINO index and precipitation (shown in Table 3).

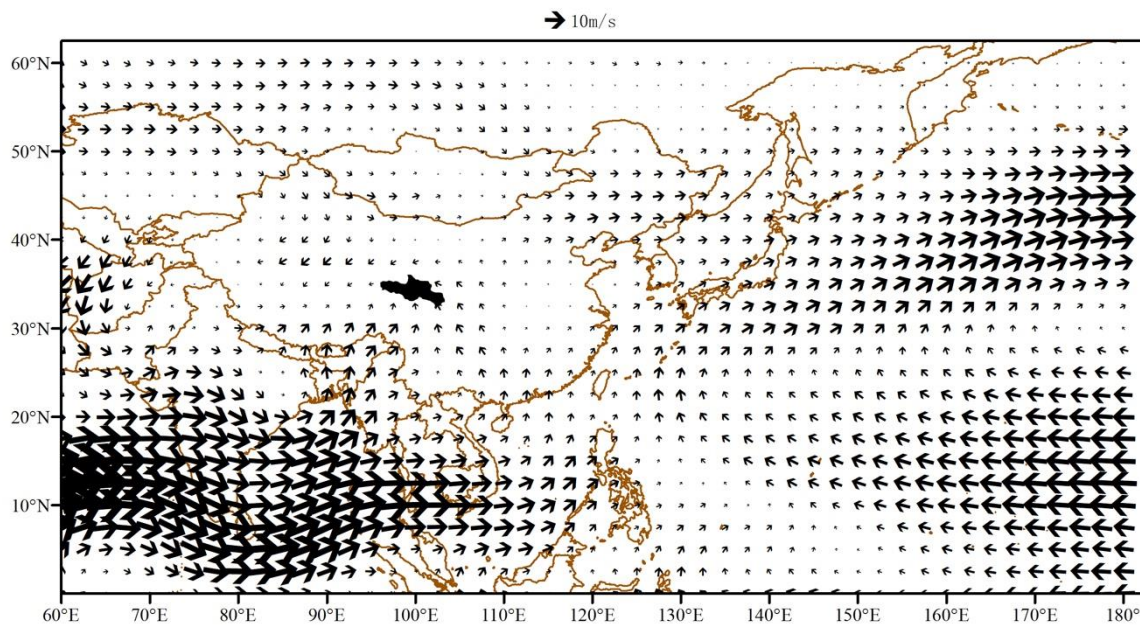


Figure 7. Composites of the 850-mb vector wind from June to September for the period of 1961–2015. Arrows indicate the wind direction and speed. The shade area indicates the study area.

4. Conclusions

The spatiotemporal trend and variability of precipitation extremes in the SRYR were examined using selected indices of daily precipitation data from 1961 to 2015. The Mann-Kendall test was used to explore spatial patterns of change. SVD was conducted to identify linkages between precipitation extremes in the SRYR and global teleconnection patterns. The 850-mb vector wind from June to September for the period 1961–2015 was explored for possible physical mechanisms. It was found that spatiotemporal variability of precipitation extremes is greatly affected by the south-easterly summer monsoon, and a significant increasing/decreasing trend was noticed from the northwest to the southeast part. Statistically significant trends were not found for the majority of the stations and the six precipitation extreme indices. Instead, the trend of precipitation extremes varies at different stations. Regional analysis showed that both CDD and CWD, indicating precipitation persistence, show decreasing trends with -2.3 and -0.2 days/decades, respectively. The other four indices have slightly increasing trends. SVD was used on the cross-covariance matrix of the precipitation extremes and climate indices datasets. The SVD results verified the linkages between some of the climate indices and precipitation extremes in the SRYR. The first two modes of SVD were elaborated on in detail since they can be linked with teleconnection patterns. The findings indicated that five precipitation extreme indices are negatively related to the ENSO, and CDD is positively linked with the Scandinavian pattern. It can be pointed out that the southwestern monsoon from the Indian Ocean brings plentiful moisture to the region. Furthermore, the anti-cyclone in the western part of North Pacific (WNP) contributes to the transport of moisture to the SRYR. The above findings have major implications for flood and drought control in the basin.

Author Contributions: Conceptualization, F.Y. and J.L.; methodology, Q.C.; software, Y.D.; validation, H.W., D.A. and R.B.; resources, Z.H.; writing—original draft preparation, F.Y.; writing—review and editing, R.B.; funding acquisition, J.L. All authors have read and agreed to the published version of the manuscript.

Funding: The research is supported by the Open Research Fund of State Key Laboratory of Simulation and Regulation of Water Cycle in River Basin, the China Institute of Water Resources and Hydropower Research, Grant No. IWHR-SKL-KF201819. Funding from the Fundamental Research Funds for the Central Universities (Grant No. 2018B58914) and the China Postdoctoral Science Foundation (Grant No. 2018M632223) are gratefully acknowledged. Support from the National Key Research Projects (Grant No. 2018YFC1508001) is appreciated.

Conflicts of Interest: The authors declare no conflict of interest.

References

1. Liang, S.; Ge, S.; Wan, L.; Zhang, J. Can climate change cause the Yellow River to dry up? *Water Resour. Res.* **2010**, *46*. [[CrossRef](#)]
2. Yang, T.; Zhang, Q.; Chen, Y.D.; Tao, X.; Xu, C.-Y.; Chen, X. A spatial assessment of hydrologic alteration caused by dam construction in the middle and lower Yellow River, China. *Hydrol. Process.* **2008**, *22*, 3829–3843. [[CrossRef](#)]
3. Wang, X.Y.; Yang, T.; Wortmann, M.; Shi, P.F.; Hattermann, F.; Lobanova, A.; Aich, V. Analysis of multi-dimensional hydrological alterations under climate change for four major river basins in different climate zones. *Clim. Chang.* **2017**, *141*, 483–498. [[CrossRef](#)]
4. Zheng, H.X.; Zhang, L.; Liu, C.M.; Shao, Q.X.; Fukushima, Y. Changes in stream flow regime in headwater catchments of the Yellow River basin since the 1950s. *Hydrol. Process.* **2007**, *21*, 886–893. [[CrossRef](#)]
5. Allan, R.P.; Soden, B.J. Atmospheric warming and the amplification of precipitation extremes. *Science* **2008**, *321*, 1481–1484. [[CrossRef](#)] [[PubMed](#)]
6. Aguilar, E.; Barry, A.A.; Brunet, M.; Ekang, L.; Fernandes, A.; Massoukina, M.; Mbah, J.; Mhanda, A.; do Nascimento, D.J.; Peterson, T.C.; et al. Changes in temperature and precipitation extremes in western central Africa, Guinea Conakry, and Zimbabwe, 1955–2006. *J. Geophys. Res. Atmos.* **2009**, *114*. [[CrossRef](#)]
7. Yu, Z.; Jiang, P.; Gautam, M.R.; Zhang, Y.; Acharya, K. Changes of seasonal storm properties in California and Nevada from an ensemble of climate projections. *J. Geophys. Res. Atmos.* **2015**, *120*, 2676–2688. [[CrossRef](#)]
8. Casanueva, A.; Rodriguez-Puebla, C.; Frias, M.D.; Gonzalez-Reviriego, N. Variability of extreme precipitation over Europe and its relationships with teleconnection patterns. *Hydrol. Earth Syst. Sci.* **2014**, *18*, 709–725. [[CrossRef](#)]
9. Yang, T.; Wang, X.Y.; Yu, Z.B.; Krysanova, V.; Chen, X.; Schwartz, F.W.; Sudicky, E.A. Climate change and probabilistic scenario of streamflow extremes in an alpine region. *J. Geophys. Res. Atmos.* **2014**, *119*, 8535–8551. [[CrossRef](#)]
10. Yang, T.; Wang, X.Y.; Zhao, C.Y.; Chen, X.; Yu, Z.B.; Shao, Q.X.; Xu, C.Y.; Xia, J.; Wang, W.G. Changes of climate extremes in a typical arid zone: Observations and multimodel ensemble projections. *J. Geophys. Res. Atmos.* **2011**, *116*. [[CrossRef](#)]
11. Luo, P.; Mu, D.; Xue, H.; Ngo-Duc, T.; Dang-Dinh, K.; Takara, K.; Nover, D.; Schladow, G. Flood inundation assessment for the Hanoi Central Area, Vietnam under historical and extreme rainfall conditions. *Sci. Rep.* **2018**, *8*, 12623. [[CrossRef](#)] [[PubMed](#)]
12. Luo, P.; Zhou, M.; Deng, H.; Lyu, J.; Cao, W.; Takara, K.; Nover, D.; Geoffrey Schladow, S. Impact of forest maintenance on water shortages: Hydrologic modeling and effects of climate change. *Sci. Total Environ.* **2018**, *615*, 1355–1363. [[CrossRef](#)] [[PubMed](#)]
13. Yuan, F.; Berndtsson, R.; Uvo, C.B.; Zhang, L.; Jiang, P. Summer precipitation prediction in the source region of the Yellow River using climate indices. *Hydrol. Res.* **2015**, *47*, 847–856. [[CrossRef](#)]
14. Hatzaki, M.; Lingis, P.; Flocas, H.A.; Michaelides, S.; Oikonomou, C. The impact of an upper tropospheric teleconnection pattern on precipitation extremes over Cyprus. *Adv. Geosci.* **2008**, *16*, 131–136. [[CrossRef](#)]
15. Leathers, D.J.; Yarnal, B.; Palecki, M.A. The Pacific North-American teleconnection pattern and United-States climate. 1. Regional temperature and precipitation associations. *J. Clim.* **1991**, *4*, 517–528. [[CrossRef](#)]
16. Boulanger, J.P.; Leloup, J.; Penalba, O.; Rusticucci, M.; Lafon, F.; Vargas, W. Observed precipitation in the Parana-Plata hydrological basin: Long-term trends, extreme conditions and ENSO teleconnections. *Clim. Dyn.* **2005**, *24*, 393–413. [[CrossRef](#)]

17. Back, L.E.; Bretherton, C.S. The relationship between wind speed and precipitation in the Pacific ITCZ. *J. Clim.* **2005**, *18*, 4317–4328. [[CrossRef](#)]
18. Kidson, J.W.; Newell, R.E. African rainfall and its relation to the upper air circulation. *Quart. J. R. Meteorol. Soc.* **1977**, *103*, 441–456. [[CrossRef](#)]
19. Zhou, W.; Chan, J.C.L. ENSO and the South China Sea summer monsoon onset. *Int. J. Climatol.* **2007**, *27*, 157–167. [[CrossRef](#)]
20. Zhang, W.J.; Jin, F.F.; Stuecker, M.F.; Wittenberg, A.T.; Timmermann, A.; Ren, H.L.; Kug, J.S.; Cai, W.J.; Cane, M. Unraveling El Niño's impact on the East Asian Monsoon and Yangtze River summer flooding. *Geophys. Res. Lett.* **2016**, *43*, 11375–11382. [[CrossRef](#)]
21. Yuan, F.F.; Berndtsson, R.; Zhang, L.; Uvo, C.B.; Hao, Z.C.; Wang, X.P.; Yasuda, H. Hydro climatic trend and periodicity for the source region of the yellow river. *J. Hydrol. Eng.* **2015**, *20*, 05015003. [[CrossRef](#)]
22. Zheng, H.X.; Zhang, L.; Zhu, R.R.; Liu, C.M.; Sato, Y.; Fukushima, Y. Responses of streamflow to climate and land surface change in the headwaters of the Yellow River Basin. *Water Resour. Res.* **2009**, *45*. [[CrossRef](#)]
23. Tang, Q.H.; Oki, T.; Kanae, S.; Hu, H.P. Hydrological cycles change in the Yellow River basin during the last half of the twentieth century. *J. Clim.* **2008**, *21*, 1790–1806. [[CrossRef](#)]
24. Tian, Q.; Prange, M.; Merkel, U. Precipitation and temperature changes in the major Chinese river basins during 1957–2013 and links to sea surface temperature. *J. Hydrol.* **2016**, *536*, 208–221. [[CrossRef](#)]
25. Zhang, Z.X.; Jin, Q.; Chen, X.; Xu, C.Y.; Jiang, S.S. On the linkage between the extreme drought and pluvial patterns in China and the large-scale atmospheric circulation. *Adv. Meteorol.* **2016**. [[CrossRef](#)]
26. Yuan, F.F.; Yasuda, H.; Berndtsson, R.; Uvo, C.B.; Zhang, L.N.; Hao, Z.C.; Wang, X.P. Regional sea-surface temperatures explain spatial and temporal variation of summer precipitation in the source region of the Yellow River. *Hydrol. Sci. J.* **2016**, *61*, 1383–1394. [[CrossRef](#)]
27. Liu, H.; Duan, K.; Li, M.; Shi, P.; Yang, J.; Zhang, X.; Sun, J. Impact of the North Atlantic Oscillation on the Dipole Oscillation of summer precipitation over the central and eastern Tibetan Plateau. *Int. J. Climatol.* **2015**. [[CrossRef](#)]
28. Rana, A.; Uvo, C.B.; Bengtsson, L.; Sarthi, P.P. Trend analysis for rainfall in Delhi and Mumbai, India. *Clim. Dyn.* **2012**, *38*, 45–56. [[CrossRef](#)]
29. Tootle, G.A.; Piechota, T.C. Relationships between Pacific and Atlantic ocean sea surface temperatures and US streamflow variability. *Water Resour. Res.* **2006**, *42*. [[CrossRef](#)]
30. Krichak, S.O.; Breitgand, J.S.; Gualdi, S.; Feldstein, S.B. Teleconnection-extreme precipitation relationships over the Mediterranean region. *Theor. Appl. Climatol.* **2014**, *117*, 679–692. [[CrossRef](#)]
31. Wang, B.; Wu, R.G.; Fu, X.H. Pacific-East Asian teleconnection: How does ENSO affect East Asian climate? *J. Clim.* **2000**, *13*, 1517–1536. [[CrossRef](#)]
32. Zhang, Q.; Xu, C.Y.; Zhang, Z.X.; Chen, Y.Q.D.; Liu, C.L.; Lin, H. Spatial and temporal variability of precipitation maxima during 1960–2005 in the Yangtze River basin and possible association with large-scale circulation. *J. Hydrol.* **2008**, *353*, 215–227. [[CrossRef](#)]
33. Hellstrom, C. Atmospheric conditions during extreme and non-extreme precipitation events in Sweden. *Int. J. Climatol.* **2005**, *25*, 631–648. [[CrossRef](#)]
34. Yang, T.; Shao, Q.X.; Hao, Z.C.; Chen, X.; Zhang, Z.X.; Xu, C.Y.; Sun, L.M. Regional frequency analysis and spatio-temporal pattern characterization of rainfall extremes in the Pearl River Basin, China. *J. Hydrol.* **2010**, *380*, 386–405. [[CrossRef](#)]
35. Lan, Y.C.; Zhao, G.H.; Zhang, Y.N.; Wen, J.; Liu, J.Q.; Hu, X.L. Response of runoff in the source region of the Yellow River to climate warming. *Quat. Int.* **2010**, *226*, 60–65. [[CrossRef](#)]
36. Hu, Y.; Maskey, S.; Uhlenbrook, S. Trends in temperature and rainfall extremes in the Yellow River source region, China. *Clim. Chang.* **2012**, *110*, 403–429. [[CrossRef](#)]
37. Washington, R.; Hodson, A.; Isaksson, E.; MacDonald, O. Northern Hemisphere teleconnection indices and the mass balance of Svalbard glaciers. *Int. J. Climatol.* **2000**, *20*, 473–487. [[CrossRef](#)]
38. Barnston, A.G.; Livezey, R.E. Classification, seasonality and persistence of low-frequency atmospheric circulation patterns. *Mon. Weather Rev.* **1987**, *115*, 1083–1126. [[CrossRef](#)]
39. Karl, T.R.; Nicholls, N.; Ghazi, A. CLIVAR/GCOS/WMO Workshop on Indices and Indicators for Climate Extremes—Workshop summary. *Clim. Chang.* **1999**, *42*, 3–7. [[CrossRef](#)]
40. Alexander, L.V. Global observed long-term changes in temperature and precipitation extremes: A review of progress and limitations in IPCC assessments and beyond. *Weather Clim. Extrem.* **2016**, *11*, 4–16. [[CrossRef](#)]

41. Chu, P.S.; Chen, Y.R.; Schroeder, T.A. Changes in precipitation extremes in the Hawaiian Islands in a warming climate. *J. Clim.* **2010**, *23*, 4881–4900. [[CrossRef](#)]
42. Kumar, S.; Merwade, V.; Kam, J.; Thurner, K. Streamflow trends in Indiana: Effects of long term persistence, precipitation and subsurface drains. *J. Hydrol.* **2009**, *374*, 171–183. [[CrossRef](#)]
43. Harzallah, A.; DeAragao, J.O.R.; Sadourny, R. Interannual rainfall variability in north-east Brazil: Observation and model simulation. *Int. J. Climatol.* **1996**, *16*, 861–878. [[CrossRef](#)]
44. Liu, X.D.; Yanai, M. Relationship between the Indian monsoon rainfall and the tropospheric temperature over the Eurasian continent. *Quart. J. R. Meteorol. Soc.* **2001**, *127*, 909–937. [[CrossRef](#)]
45. Wallace, J.M.; Smith, C.; Bretherton, C.S. Singular Value Decomposition of Wintertime Sea-Surface Temperature and 500-Mb Height Anomalies. *J. Clim.* **1992**, *5*, 561–576. [[CrossRef](#)]
46. Uvo, C.B.; Repelli, C.A.; Zebiak, S.E.; Kushnir, Y. The relationships between tropical Pacific and Atlantic SST and northeast Brazil monthly precipitation. *J. Clim.* **1998**, *11*, 551–562. [[CrossRef](#)]
47. Bretherton, C.S.; Smith, C.; Wallace, J.M. An Intercomparison of methods for finding coupled patterns in climate data. *J. Clim.* **1992**, *5*, 541–560. [[CrossRef](#)]
48. Fu, G.B.; Yu, J.J.; Yu, X.B.; Ouyang, R.L.; Zhang, Y.C.; Wang, P.; Liu, W.B.; Min, L.L. Temporal variation of extreme rainfall events in China, 1961–2009. *J. Hydrol.* **2013**, *487*, 48–59. [[CrossRef](#)]
49. Dong, Q.; Chen, X.; Chen, T.X. Characteristics and changes of extreme precipitation in the yellow-huaihe and yangtze-huaihe rivers basins, China. *J. Clim.* **2011**, *24*, 3781–3795. [[CrossRef](#)]
50. Wang, W.G.; Shao, Q.X.; Yang, T.; Peng, S.Z.; Yu, Z.B.; Taylor, J.; Xing, W.Q.; Zhao, C.P.; Sun, F.C. Changes in daily temperature and precipitation extremes in the Yellow River Basin, China. *Stoch. Environ. Res. Risk Assess.* **2013**, *27*, 401–421. [[CrossRef](#)]
51. Li, Z.; Zheng, F.L.; Liu, W.Z.; Flanagan, D.C. Spatial distribution and temporal trends of extreme temperature and precipitation events on the Loess Plateau of China during 1961–2007. *Quat. Int.* **2010**, *226*, 92–100. [[CrossRef](#)]
52. Bueh, C.; Nakamura, H. Scandinavian pattern and its climatic impact. *Quart. J. R. Meteorol. Soc.* **2007**, *133*, 2117–2131. [[CrossRef](#)]
53. Zhang, J. Low temperature in the northeastern China and heavy snowstorm over Inner Mongolia and Xinjiang. *Mon. Meteorol.* **2001**, *27*, 62–63. (In Chinese)
54. Liu, Y.Y.; Wang, L.; Zhou, W.; Chen, W. Three Eurasian teleconnection patterns: Spatial structures, temporal variability, and associated winter climate anomalies. *Clim. Dyn.* **2014**, *42*, 2817–2839. [[CrossRef](#)]
55. Fan, L.; Shin, S.-I.; Liu, Q.; Liu, Z. Relative importance of tropical SST anomalies in forcing East Asian summer monsoon circulation. *Geophys. Res. Lett.* **2013**, *40*, 2471–2477. [[CrossRef](#)]
56. Huang, R.; Chen, W.; Yang, B.; Zhang, R. Recent advances in studies of the interaction between the East Asian winter and summer monsoons and ENSO cycle. *Adv. Atmos. Sci.* **2004**, *21*, 407–424.
57. Feng, J.; Chen, W.; Tam, C.Y.; Zhou, W. Different impacts of El Niño and El Niño Modoki on China rainfall in the decaying phases. *Int. J. Climatol.* **2011**, *31*, 2091–2101. [[CrossRef](#)]
58. Huang, C.C.; Pang, J.; Zha, X.; Su, H.; Jia, Y.; Zhu, Y. Impact of monsoonal Clim. Chang. on Holocene overbank flooding along Sushui River, middle reach of the Yellow River, China. *Quat. Sci. Rev.* **2007**, *26*, 2247–2264. [[CrossRef](#)]
59. Liu, Q.; Yang, Z.; Cui, B. Spatial and temporal variability of annual precipitation during 1961–2006 in Yellow River Basin, China. *J. Hydrol.* **2008**, *361*, 330–338. [[CrossRef](#)]
60. Tedeschi, R.G.; Cavalcanti, I.F.A.; Grimm, A.M. Influences of two types of ENSO on South American precipitation. *Int. J. Climatol.* **2013**, *33*, 1382–1400. [[CrossRef](#)]
61. Cai, W.; Van Rensch, P.; Cowan, T.; Sullivan, A. Asymmetry in ENSO teleconnection with regional rainfall, its multidecadal variability, and impact. *J. Clim.* **2010**, *23*, 4944–4955. [[CrossRef](#)]
62. Black, E.; Slingo, J.; Sperber, K.R. An observational study of the relationship between excessively strong short rains in coastal East Africa and Indian Ocean SST. *Mon. Weather Rev.* **2003**, *131*, 74–94. [[CrossRef](#)]
63. Chang, C.; Harr, P.; Ju, J. Possible roles of Atlantic circulations on the weakening Indian monsoon rainfall–ENSO relationship. *J. Clim.* **2001**, *14*, 2376–2380. [[CrossRef](#)]
64. Zhang, R.; Li, T.; Wen, M.; Liu, L. Role of intraseasonal oscillation in asymmetric impacts of El Niño and La Niña on the rainfall over southern China in boreal winter. *Clim. Dyn.* **2014**, *45*, 559–567. [[CrossRef](#)]
65. Onyutha, C.; Willems, P. Spatial and temporal variability of rainfall in the Nile Basin. *Hydrol. Earth Syst. Sci.* **2015**, *19*, 2227–2246. [[CrossRef](#)]

66. Wu, R.G.; Hu, Z.Z.; Kirtman, B.P. Evolution of ENSO-related rainfall anomalies in East Asia. *J. Clim.* **2003**, *16*, 3742–3758. [[CrossRef](#)]
67. Wang, H.; Yang, Z.; Saito, Y.; Liu, J.P.; Sun, X. Interannual and seasonal variation of the Huanghe (Yellow River) water discharge over the past 50 years: Connections to impacts from ENSO events and dams. *Glob. Planet. Chang.* **2006**, *50*, 212–225. [[CrossRef](#)]
68. Achuthavarier, D.; Krishnamurthy, V.; Kirtman, B.P.; Huang, B. Role of the Indian ocean in the ENSO–Indian summer monsoon teleconnection in the NCEP climate forecast system. *J. Clim.* **2012**, *25*, 2490–2508. [[CrossRef](#)]
69. Ashok, K.; Guan, Z.; Yamagata, T. Impact of the Indian Ocean dipole on the relationship between the Indian monsoon rainfall and ENSO. *Geophys. Res. Lett.* **2001**, *28*, 4499–4502. [[CrossRef](#)]
70. Feng, S.; Hu, Q. Variations in the teleconnection of ENSO and summer rainfall in northern China: A role of the Indian summer monsoon. *J. Clim.* **2004**, *17*, 4871–4881. [[CrossRef](#)]



© 2020 by the authors. Licensee MDPI, Basel, Switzerland. This article is an open access article distributed under the terms and conditions of the Creative Commons Attribution (CC BY) license (<http://creativecommons.org/licenses/by/4.0/>).